Research Square

Preprints are preliminary reports that have not undergone peer review.
They should not be considered conclusive, used to inform clinical practice,
or referenced by the media as validated information.

Bulk Superconductivity driven by Disorder-Induced Delocalization

James Analytis

analytis@berkeley.edu

University of California, Berkeley https://orcid.org/0000-0002-7657-7688

Lu Chen

University of Illinois Urbana-Champaign https://orcid.org/0000-0002-0407-9209

Sae Hee Ryu

Korea Basic Science Institute https://orcid.org/0000-0003-3207-7582

Avior Almoalem

University of Illinois at Urbana Champaign https://orcid.org/0000-0001-8462-0829

Yuanqi Lyu

UC Berkeley https://orcid.org/0000-0002-7732-1094

Koh Yamakawa

University of california Berkeley

Luke Cairns

University of California, Berkeley

Ryan Day

University of california Berkeley

Ehud Altman

University of California Berkeley

Daniel Podolsky

Technion - Israel Institute of Technology https://orcid.org/0000-0001-6428-2957

Dung-Hai Lee

University of California, Berkeley https://orcid.org/0000-0002-4793-5829

Vidya Madhavan

University of Illinois at Urbana Champaign https://orcid.org/0000-0002-3112-9734

Eli Rotenberg

E. O. Lawrence Berkeley National Laboratory https://orcid.org/0000-0002-3979-8844

Article

Keywords:

Posted Date: October 7th, 2026

DOI: https://doi.org/10.21203/rs.3.rs-11118768/v1

License: This work is licensed under a Creative Commons Attribution 4.0 International License.
Read Full License

Additional Declarations: There is **NO** Competing Interest.

Bulk Superconductivity driven by Disorder-Induced Delocalization

Lu Chen[1,2,3,*], Sae-Hee Ryu[4,*], Avior Almoalem[3], Yuanqi Lyu[2], Koh Yamakawa[2], Luke Pritchard Cairns[2], Ryan Day[2], Ehud Altman[2], Daniel Podolsky[5], Dung-Hai Lee[1,2], Vidya Madhavan[3], Eli Rotenberg[4] & James G. Analytis[1,2,6,7]

[1]*Materials Science Division, Lawrence Berkeley National Laboratory, Berkeley, CA 94720, USA*
[2]*Department of Physics, University of California, Berkeley, California 94720, USA*
[3]*Department of Physics, University of Illinois Urbana-Champaign 61801, USA*
[4]*Advanced Light Source, Lawrence Berkeley National Laboratory, Berkeley, CA 94720, USA*
[5]*Physics Department, Technion, Haifa 32000, Israel*
[6]*CIFAR Quantum Materials, CIFAR, Ontario, Toronto M5G 1M1, Canada*
[7]*Kavli Energy NanoScience Institute, Berkeley, California 94720, USA*

Delocalization transitions underlie many important problems in condensed matter physics, particularly unconventional superconductivity. The observation is that a system near a localized state (like a Mott or Kondo insulator), undergoes a small to large Fermi surface change that coincides with the highest superconducting critical temperatures. The implication is that understanding the mechanism behind the delocalization will point to the mechanism of superconductivity itself [1; 2; 3]. We explore this question in the unconventional superconductor 4Hb-TaS_2, a system that interleaves Mott-like and metallic layers, and show that there is indeed a Fermi surface transition in a flat band that is correlated with the appearance of bulk superconductivity. We show that there is a surprising origin to this delocalization: disorder. Although counter-intuitive at first, we explain that this process may be more common in nature than previously thought.

In many classes of unconventional superconductors, it is often found that a non-thermal tuning parameter like pressure, doping or electric field, can continuously transition the electronic system from a localized to a delocalized state. In this process, the interplay of disorder and quantum order plays a key role, spanning problems from understanding how high-temperature superconductivity is connected to the strange metal [4], to how Anderson localization is connected to spin liquids [5]. The tension is that disorder is usually understood to have a localizing effect on itinerant electrons, destroying quasiparticle coherence without which it is hard to understand how the materials remain metals let alone become superconductors. It is of special interest therefore, to study superconductors where disorder and delocalization work in harmony rather than in opposition.

The material TaS_2 is an exemplary system where different lattice structures can host very different quantum ground states [6; 7; 8]; it forms in multiple structural polytypes $1T$, $2H$, or $4Hb$-TaS_2 etc., and manifests various charge density wave (CDW) orders [6], superconductivity [6], Mott physics [9], and potentially a quantum spin liquid phase [10; 11]. In such a system, structural disorder should be expected to have a significant effect on the quantum order of the

system.

Compared to the $1T$- and $2H$- polytypes of TaS_2, $4Hb$-TaS_2 has attracted tremendous attention recently because its structure represents a natural interleaving of the $1T$ and $1H$ layers (as shown in Fig. 1 (a)), combining key structural and electronic features of both a Mott insulator and a superconductor [12]. The former provides a localized 'flat band' subsystem, while the latter provides a sea of itinerant charge carriers, meeting in three-dimensionally stacked interfaces. Superconductivity with a transition temperature in the range of 2.7 - 3 K has been observed. A number of unconventional properties, including time reversal symmetry breaking [13], topological boundary modes [14], spontaneous vortices [15], and multi-component order parameters [16; 17], have also been reported recently.

However, the connection of the superconducting order to the parent Mott and metallic normal state remains opaque. In this study we show that the presence of superconductivity in $4Hb$-TaS_2 is strongly connected to disorder-driven delocalization of carriers in the T-layer, while the suppression of the CDW in the H-layer is, by comparison, a relatively small effect. We suggest that it is the fragility of the flat band that is the primary culprit, and this allows small amounts of disorder to liberate carriers and create a new Fermi surface that facilitates superconductivity. We suggest a simple mechanism that is so general that it could manifest in different materials, and may therefore help understand other unconventional superconductors where a delocalization transition is tied to the appearance of superconductivity.

To create disorder in $4Hb$-TaS_2, we substitute sulfur with isovalent selenium, so the primary effect is local structural distortion in the material without substantially changing the carrier density. Our evidence, shown in Supplementary Materials Sec. S2, indicates Se defects behave well in $4Hb$-$Ta(S_{1-x}Se_x)_2$, substituting randomly for S in both T and H layers and not taking unusual interstitial positions, clustering, or unexpected chemical bonding. The resistivity curves for three samples of $4Hb$-$Ta(S_{1-x}Se_x)_2$, at x = 0%, 0.25% and 1% are shown in Figure 1 (b). The pristine samples have very long mean free paths, which can be observed in the residual resistivity ratio which evolves by more than an order of magnitude from $\rho_{300}/\rho_{T_{c+}} = 66$ at x = 0% to $\rho_{300}/\rho_{T_{c+}} = 5$ at $x = 1\%$, where T_{c+} is defined as the normal state temperature just above T_c. The latter residual resistivity ratio is much more typical of samples presented in the literature [18; 19], and the high mobility samples presented here (x = 0%) will play an important role in understanding the underlying physics of these materials as argued below. As can be seen in Figure 1 (b), all samples show evidence for the incommensurate CDW (ICCDW) appearing above room temperature, which is known to be the Star-of-David (SOD) ordering with approximately $\sqrt{(13)} \times \sqrt{(13)}R13.9^\circ$ (henceforth $\sqrt{13}$) symmetry in the 1T layers [20].

The trend in resistivity is very typical, increasing monotonically with Se disorder, but the trend in the magnetization is puzzling by comparison. As shown in Fig. 1 (c), the onset of superconductivity occurs at temperatures as high as $T_c = 3.5$ K for the x = 0.25 % sample, whereas the

x = 1 % sample shows an onset at $\sim$ 3 K. However, the most important observation is the striking contrast of the volume fraction with the pristine samples. These data show a vanishingly small volume fraction of superconductivity, less than 0.6%, whereas just a small amount of Se brings up the volume fraction to 80%. (Given the demagnetization factor of the sample, the volume-metric fraction in the Se-substituted sample is unitary.) It has been noticed before that Se-free samples show a smaller volume fraction [19], but here the trend is stark: small amounts of disorder increase the volume fraction by more than two orders of magnitude.

In Figure 2, we show the Hall coefficient $R_H(H)$ as a function of magnetic field for x = 0% and 1%. (See Supplementary Materials Sec. S1 for raw $\rho_{xy}(H)$ all compositions.) Due to the CDW reconstruction, the Fermi surface of the $4Hb$-Ta($S_{1-x}Se_x)_2$ system is quite complicated, making the interpretation of the Hall number challenging. However, the high field limit is well defined in any multi-band system, and is simply the difference between the number of electrons and the number of holes, $R_H(\infty) = -1/e(n_e - n_h)$. Experimentally, this regime is identified by a saturation in $R_H(H)$, flat-lining at $R_H(\infty)$. At high temperatures ($T \sim$ 100 K), the samples are very well behaved, with x = 0% and 1% showing an essentially unchanged Hall number. Interestingly, $R_H(\infty)$ for $4Hb$-Ta($S_{1-x}Se_x)_2$ is just under double that of $R_H(\infty)$ for the $2H-TaS_2$, consistent with the expected localization of the $1T$ layers, which account for half of the $4Hb$ structure.

At lower temperatures ($T \sim$ 5 K), the evolution of R_H with x is dramatic. The pristine $4Hb$-TaS_2 sample continues the expected trend, exhibiting a value of $R_H(\infty)$ that is approximately twice that of the $2H-$ structure and with the same sign. However, as soon as a small amount of Se is added, there is a striking change: not only is there a sign change in the Hall coefficient, but the approach to the high-field limit changes qualitatively and quantitatively. (The $2H$-TaS_2 has been reported to show similar behavior as a function of thickness, which may also be related to disorder/strain [21].) For x = 1% sample, the Hall number is large at low fields and decreases at high fields, approaching a value corresponding to a significantly higher carrier density. However, we do not reach the high-field limit, emphasizing that the Fermi surfaces are indeed very different from the pristine case. For x = 0% we observe $n_e - n_h \approx 2 \times 10^{21}$ cm^{-3}.

Although small quantities of defects do not, in general, significantly affect the Fermi surface of metals, the dramatic changes we observe are difficult to explain in a different scenario. To gain further insight, we turn to spatially-resolved ARPES [13; 22; 23; 24; 25; 26; 27; 28; 29; 25], a probe which is directly sensitive to interlayer charge transfer, lattice symmetries, orbital order, and band renormalization due to interactions. Fig. 3 (a) shows the μARPES electronic structure of T-terminated surfaces for $4Hb$-TaS_2 with 0% Se. Although not evident at E_F, replica bands observed at higher binding energy prove that the T-layer for all samples presented is in the $\sqrt{13}$ reconstructed phase associated with the CDW formation and SOD cluster arrangement. Overlaid on the data is a tight-binding (TB) model for an isolated H-layer (see Supplementary Materials Sec. S3). Its close match to the measured bands establishes that the Fermi surface observed on the T-terminated surface of the 0% sample (denoted "0%I") exhibits only the features associated with the underlying H-layer. This shows that the surface T-layer is insulating.

Fig. 3(b) shows the T-surface Fermi surface for 1% Se-doped samples. In addition to the H-layer-derived band features exhibited by the $0\%I$ samples in (a), a new set of sharp metallic "windmill" states appears around Γ. Although recent studies have attributed these chiral windmill features directly to the T-layer flat band [23; 24], their dispersion indicates they are actually replica bands of the underlying H-layer folded by the $\sqrt{13}$ lattice superpotential [25]. Crucially, these itinerant H-layer replica states hybridize with the T-layer flat band, which has been interpreted previously as a metallic Kondo-like resonance at $E_{\rm F}$ [25; 30]. Similar states are apparent in samples with 0.25% Se concentration (not shown here). Because these T-surfaces are metallic, the Se-doped samples are designated as $1\%M$ and $0.25\%M$, respectively. The emergence of this new, delocalized Fermi surface on the T-layer makes sense of the dramatic changes observed in the size and amplitude of the high-field Hall coefficient.

All H layers (Fig. 3(c,d)) show signatures of 3×3 CDW reconstruction, evidenced by strongly reduced intensity along the hole pockets around the K points and the "dog-bone" pockets near the M points of the Brillouin Zone. Quantitative analysis of the H-layer Fermi-surface areas reveals a finite charge transfer from the T to H layers, but our extracted values remain substantially smaller than the $1\,e^-$ per SOD that would be required to fully empty the T-layer flat band (full details in Supplementary Materials Sec. S3). Specifically, for a bulk T-layer sandwiched between two $1H$ layers, the retained charge is $\sim 0.46\,e^-$/SOD in $0\%I$ samples, rising to $\sim 0.70\,e^-$/SOD with 1% Se — in both cases the flat band retains the majority of its charge. These results directly contradict a complete charge-transfer scenario and confirm that the T-layer remains partially occupied across all sample classes. We emphasize that the method for calculating the charge transfer is taken with respect to the native H-layer, and not to a reference $2H$-TaS_2 sample as done in other studies, eliminating the risk of overestimating the actual charge transfer. It then appears that Se induces a transition in this state which delocalizes the flat band, enabling the hybridization of electrons between layers, manifested by the appearance of a new Fermi surface on the T-layer.

Our STM studies of twinned and non-twinned regions of H-layer CDW domains of $0\%I$ samples confirm that the appearance of superconductivity is correlated with disorder. Figure 4 (a,d) shows the atomically resolved topography obtained on the H-layer and fast Fourier Transform (FFT) in Figure 4 (b,e) for twinned and non-twinned regions respectively. In the former, a CDW state is formed with multiple domains, manifested in real space as a local $\sim 3 \times 3$ order having a prominent stripe modulation running from lower left to upper right and period ~ 7 nm. This modulated CDW appears in k-space by split peaks near the 3×3 Bragg peaks in Fig. 4 (b) [31; 32], which is absent in non-twinned regions, Fig. 4 (e). Additional, weaker Bragg peaks, most notably a central hexagon ring (white arrows), in the FFT correspond to additional Moiré modulations of the CDW at scales > 4 nm that are observable in the STM map due to the T-layer immediately below. These are absent in the non-twinned regions. Fig. 4(c,f) shows a striking difference in the superconducting signatures between the two regions: while twinned regions have a well-defined superconducting gap, this is strongly suppressed in areas with a single CDW domain. We do not have equivalent data on T-layers, but this does not affect the main observation that the only regions where superconductivity can be found in $0\%I$ samples, are regions where there is twinning and

disorder. This naturally answers why pristine samples have a substantially smaller superconducting volume fraction as compared to disordered ones.

Our results point to a surprising and counter-intuitive role of disorder in correlated metals with flat bands. Anderson localization, the main framework in which the properties of disordered metals are understood, predicts that in 3D metals extended states cannot form when the random potential is larger than the gain in kinetic energy from hopping. However, in the present situation, the ideal (clean) system, theoretically has a correlation-driven flat band in the $1T$ layers; models predict the flat band on the T-layer to be half-filled and derived from Ta d_{z^2} orbitals localized at the center of the SOD cluster [33; 9; 34], and confirmed experimentally in monolayer $1T-TaS_2$ [35; 36]. As detailed in Supplementary Materials Sec. S5, our polarization-dependent ARPES measurements explicitly confirm the d_{z^2} orbital character of these localized states, directly linking them to the persistent T-layer flat band. Hence, it might be expected that the kinetic gain of the T-layer states will be small compared to any amount of disorder, bringing into sharp focus the question of what drives the delocalization we observe.

This brings us to the role of the H-layers. Recently, it was proposed that massive interlayer charge transfer completely depletes the flat band in the heterostructure, effectively destroying the Mott physics [22; 23]. However, our data explicitly contradict this: in our pristine $0\%I$ samples, the $1T$-layer's flat band is not completely depleted, but remains at least partially occupied. This is evidenced by diffuse d_{z^2} states that tail up to E_{F} with a maximum intensity around E_{F}-25 meV. The T-layer can remain localized even when directly next to a H-layer, and it is only when disorder is also present that the T-layer states are delocalized. The proximity of the H-layer is, therefore, a necessary but not sufficient condition; it is disorder that helps make the d_{z^2} states itinerant.

We propose that weak Se substitution destabilizes the partially localized $1T$ flat-band state by enhancing bandwidth and charge fluctuations, thereby driving a correlation-induced delocalization transition. There are two likely cooperating correlation mechanisms for Se's outsized effect on the T-layer. First, Se introduces significant p-d hybridization between its Se $4p$ and Ta $5d$ orbitals that is absent when S occupies the chalcogen site [37; 38]; this increases the effective T-layer bandwidth W and reduces the ratio U/W governing the Mott-like physics [38], directly enabling the delocalization transition evidenced by ARPES, the Hall coefficient, and the violation of the Wiedemann-Franz law (as shown in Supplementary Materials Sec. S7). Second, Se will introduce significant local deformation due to the different bond lengths, which effectively changes the local interlayer stacking with the H layers, and this is known to affect the electronic structure [39]. Once the T-layer becomes metallic, there is substantial energy to be gained through hybridization of the itinerant T-layer states with the H-layer replica bands folded by the $\sqrt{13}$ superpotential, opening gaps across large regions of k-space. This condensation energy competes directly with the electrostatic driving force for $T \rightarrow H$ charge transfer, further stabilizing the occupied flat band and making the metallic hybridized ground state self-reinforcing once reached. This second mechanism must be present with all kinds of disorder capable of destabilizing the flat band in the T-layer, even in nominally pure sulfur compounds, because it only depends on the local stacking

with the H-layers. In this way, the system not only circumvents Anderson localization, but brings new states into the Fermi sea.

The remarkable sensitivity to Se substitution does not preclude competition between the commensurate CDW and superconducting order parameters as previously suggested [13; 19], but neither does it require it. Rather, it is the fragility of the flat band that liberates carriers that can then become superconducting, while the CDW in the H-layer experiences a much weaker effect with only minor changes to the Fermi surface. This means that native disorder can similarly destroy the flat band, and so even samples sans Se may exhibit signatures of superconductivity, albeit with a volume fraction that depends on the extent of disorder (see Supplementary Materials sec. S4) [19]. Importantly, in early experiments on $4Hb$-TaS_2, which worked with samples of substantially higher quality than those generally studied today, superconductivity does not appear to be present [40]. Finally, although the specific mechanism by which disorder affects electronic structure will vary between materials, the tendency to cause delocalization that favors superconductivity may be quite general [41; 42]. For example, spatial fluctuations in systems near localization theoretically lead to locally boosted T_c [43], have been suggested to explain strange metal behavior and the evolution of the superconductivity in unconventional superconductors [4], and could make sense of local pairing scenarios [44; 45]. The case of $4Hb$-TaS_2 is therefore unlikely to be unique, but simply provides one of the clearest examples where we can study how disorder can drive superconductivity near a delocalization transition.

Methods

Samples $4Hb$-$Ta(S_{1-x}Se_x)_2$ single crystals are synthesized by chemical vapor transport (CVT) method with iodine as a transport agent [12]. Stoichiometric amounts of Ta (Alfa Aesar 99.98%), S (ThermoFisher Scientific 99.999%), and Se (ThermoFisher Scientific 99.999%) powders are mixed and sealed inside a quartz ampoule under vacuum. The precursor is synthesized by heating up the mixture at 900 °C for 84 hours and then slowly cooling it down to room temperature. Then the obtained precursor and iodine are mixed, ground, and sealed inside a quartz ampoule under vacuum. The mixture is heated for 27 days in a two-zone furnace, where the temperature of the source zone and growth zone are fixed at 780 °C and 680 °C, then cooled down with the furnace turned off. This process yields hexagonal-shaped bulk crystals with naturally formed sharp edges as illustrated in Fig.1 (a) with a typical length of 1 to 2 mm.

1T-TaS_2 single crystals are synthesized using CVT method with elemental Ta, and S in a stoichiometric ratio of $1:2$. The powder is mixed and ground together, then loaded into an alumina crucible with iodine and sealed under vacuum in a quartz tube. The mixture is placed in a two-zone furnace with both zones heated up to 950 °C for 6 hours to encourage nucleation. Then, the source zone is raised to 1050 °C while the growth zone is kept at 950 °C for 7 days. After that, the quartz tube is quenched in ice water, and 1T-TaS_2 single crystals are harvested.

2H-TaS_2 single crystals are synthesized using CVT method with elemental Ta and S in a

Material	Se %	L (μm)	w (μm)	t (μm)
4Hb-TaS_2	x = 0 %	281	573	63
4Hb-$TaS_{1.995}Se_{0.005}$	x = 0.25 %	358	476	124
4Hb-$TaS_{1.98}Se_{0.02}$	x = 1 %	513	1101	140
1T-TaS_2	x = 0 %	1107	1109	94
2H-TaS_2	x = 0 %	723	1538	15

Table 1: Sample information including the Se concentration level and dimensions of the contacts (length between contacts L × width w × thickness t, in μm). The Se concentration level x is defined as the number of Se atoms added per formula unit of 4Hb-TaS_2.

stoichiometric ratio of 1 : 2. The precursor is synthesized by mixing and grinding Ta and S powder, which are then loaded into an alumina crucible and sealed in a quartz tube under a partial pressure of argon. The sealed tube is heated to 400 °C and held for 6 hours, then ramped to 900 °C and held for 10 days. The resulting precursor is subsequently sealed under vacuum with iodine in a quartz tube and placed in a two-zone furnace, with both zones initially held at 850 °C for 6 hours to promote nucleation. Then, the source zone is increased to 950 °C, while the growth zone is kept at 850 °C for 10 days. Finally, the furnace is shut off and allowed to cool naturally to room temperature.

For electrical and thermal transport measurements, the bulk crystals are further thinned down to $\sim 100\ \mu m$ by exfoliation using Scotch tape. Contacts are made using silver paste and silver wires. The dimensions (length between contacts L × width w × thickness t, in μm) of all the measured samples are listed in TABLE I.

Magnetization and Transport Measurements The dc magnetic susceptibility (χ) is measured using a Quantum Design Superconducting Quantum Interference Device (SQUID) system. The in-plane electrical resistivity (ρ_{xx}) and electrical Hall resistivity (ρ_{xy}) are measured by the standard four-probe method with the electrical current in the ab plane and magnetic field along c axis in a Quantum Design Physical Property Measurement System (PPMS).

The thermal conductivity $\kappa_{\rm xx}$ and thermal Hall conductivity $\kappa_{\rm xy}$ are measured in the same samples where ρ_{xx} and ρ_{xy} are measured by applying a heat current J inside the ab plane (along the naturally formed edges of the hexagonal shape) and a magnetic field H along the crystal c axis. We define the J direction to be x and the H direction to be z. The heat current J generates a longitudinal temperature difference $\Delta T_{\rm x} = T^+ - T^-$ along x. Then the thermal conductivity $\kappa_{\rm xx}$ can be defined by

$$\kappa_{\rm xx} = \frac{J}{\Delta T_{\rm x}} \left(\frac{L}{wt} \right), \tag{1}$$

where w is the sample width, t its thickness and L the distance between T^+ and T^-. The transverse temperature difference ΔT_y is measured along the y direction. The thermal Hall conductivity $\kappa_{\rm xy}$ is

then given by

$$\kappa_{\mathrm{xy}} = -\kappa_{\mathrm{yy}} \left(\frac{\Delta T_y}{\Delta T_x} \right) \left(\frac{L}{w} \right). \tag{2}$$

In this study, we use $\kappa_{\mathrm{xx}} = \kappa_{\mathrm{yy}}$ as an approximation. More detailed discussions on crystal symmetry and an accurate measurement of κ_{yy} in a hexagonal shaped sample with a six-fold rotational symmetry can be found in Ref. [46; 47].

The thermal conductivity κ_{xx} and thermal Hall conductivity κ_{xy} are measured in a PPMS using a home-built thermal transport puck. The thermal transport measurement is carried out by a steady-state method using a one-heater and three-thermometer configuration. A resistive heater is connected to one end of the sample to provide a thermal gradient. The other end of the sample is mounted on the copper heat sink using silver paint. Both the longitudinal and transverse temperature difference, ΔT_x and ΔT_y, are measured using Cernox thermometers.

The measurement sequence is described as follows: a magnetic field of $+H$ is applied at 70 K, then the sample is cooled down to the base temperature of 2 K with a $+H$ field. The $+H$ data is taken by changing temperature in discrete steps under $+H$ field during warm up. At each temperature step, after the temperature is stabilized, the background is eliminated by subtracting the readings at the heater-off status from the heater-on status. After the $+H$ run is finished, a magnetic field of $-H$ is applied at the same temperature as the $+H$ run, i.e. at 70 K. Then the $-H$ run is carried out with the same procedure. The Cernox thermometers are calibrated in-situ using the heater-off readings at each temperature step. The contamination from κ_{xx} in κ_{xy} due to contact misalignment is removed by doing field anti-symmetrization of the transverse temperature difference ΔT_y. That is to say, ΔT_y is measured with both positive and negative magnetic fields in the same conditions, then κ_{xy} is calculated using the field anti-symmetrized ΔT_y, *i.e.* $\Delta T_y(H) = \left[\Delta T_y(T, H) - \Delta T_y(T, -H)\right]/2$.

ARPES Measurements All ARPES data were collected at the MAESTRO beamline 7 of the Advanced Light Source using the μARPES endstation with spot size typically 20 μm, energy resolution 10-20 meV, and sample temperature 10 K. Samples were cleaved *in situ* and measurements conducted at pressure $P < 3 \times 10^{-11}$ Torr. Before ARPES each sample was surveyed spatially to identify H and T-terminated surfaces according to their characteristic core level spectra. ARPES spectra were collected using a Scienta R4000 analyzer with customized deflector elements so that for each ARPES map, the X-rays and sample are in a fixed geometry.

Typically, cleaved samples expose both T- and H-terminated regions whose typical size ranges from submicron to tens of microns. Therefore the employed spatial resolution of 20 μm was appropriate to conduct comparisons between H and T terminated surfaces. We typically located these regions through rapid scans of the core levels which showed characteristic fingerprints as discussed in the supplemental section.

STM Measurements STM measurements were performed using a Unisoku STM, using chemically etched and annealed tungsten. Spectra were acquired using a standard lock-in technique at a

frequency of 907 Hz. The samples are cleaved in the plane perpendicular to the $c-$axis at temperatures of about 90 K in UHV conditions ($P \sim$ 5E-10 torr) and then immediately inserted into the head of the scanning tunneling microscope.

Acknowledgements This work was primarily funded by the U.S. DOE, Office of Science, Office of Basic Energy Sciences, Materials Sciences and Engineering Division under Contract No. DE-AC02-05CH11231 (Quantum Materials Program KC2202). S-H. R. and E. R. work was part of the QSA, supported by the U.S. Department of Energy, Office of Science, National Quantum Information Science Research Centers. This research used resources of the Advanced Light Source, which is a DOE Office of Science User Facility under contract no. DE-AC02-05CH11231. We thank Chris Jozwiak and Aaron Bostwick for stimulating discussions and assistance with beamtime at the ALS.

Author Contributions ∗These authors contributed equally: Lu Chen, Sae-Hee Ryu.

Correspondence Correspondence and requests for materials should be addressed to James G. Analytis (email: analytis@berkeley.edu) and Lu Chen (email: luchen721@berkeley.edu).

References

[1] Paschen, S. et al. Hall-effect evolution across a heavy-fermion quantum critical point. Nature **432**, 881–885 (2004). URL https://www.nature.com/articles/nature03129.

[2] Badoux, S. et al. Change of carrier density at the pseudogap critical point of a cuprate superconductor. Nature **531**, 210–214 (2016). URL https://www.nature.com/articles/nature16983.

[3] Maksimovic, N. et al. Evidence for a delocalization quantum phase transition without symmetry breaking in $CeCoIn_5$. Science **375**, 76–81 (2022). URL https://www.science.org/doi/10.1126/science.aaz4566.

[4] Patel, A. A., Guo, H., Esterlis, I. & Sachdev, S. Universal theory of strange metals from spatially random interactions. Science **381**, 790–793 (2023). URL https://www.science.org/doi/10.1126/science.abq6011.

[5] Potter, A. C., Barkeshli, M., McGreevy, J. & Senthil, T. Quantum Spin Liquids and the MetalInsulator Transition in Doped Semiconductors. Phys. Rev. Lett. **109**, 077205 (2012). URL https://link.aps.org/doi/10.1103/PhysRevLett.109.077205.

[6] Wilson, J. A., Di Salvo, F. J. & Mahajan, S. Charge-density waves in metallic, layered, transition-metal dichalcogenides. Phys. Rev. Lett. **32**, 882 (1974).

[7] Balseiro, C. A. & Falicov, L. M. Superconductivity and charge-density waves. Phys. Rev. B **20**, 4457 (1979).

[8] Sipos, B. et al. From Mott state to superconductivity in 1T-TaS_2. Nat. Mater. **7**, 960 (2008).

[9] Wang, Y. D. et al. Band insulator to Mott insulator transitions in 1T-TaS_2. Nat. Commun. **11**, 4215 (2020).

[10] Law, K. T. & Lee, P. A. 1T-TaS_2 as a quantum spin liquid. Proc. Natl. Acad. Sci. U.S.A. **114**, 6996 (2017).

[11] Yu, Y. J. et al. Heat transport study of the spin liquid candidate 1T-TaS_2. Phys. Rev. B **96**, 081111 (2017).

[12] Di Salvo, F. J., Bagley, B. G., Voorhoeve, J. M. & Waszczak, J. V. Preparation and properties of a new polytype of tantalum disulfide 4Hb-TaS_2. J. Phys. Chem. Solids **34**, 1357 (1973).

[13] Ribak, A. et al. Chiral superconductivity in the alternate stacking compound 4Hb-TaS_2. Sci. Adv. **6**, eaax9480 (2020).

[14] Nayak, A. K. et al. Evidence of topological boundary modes with topological nodal-point superconductivity. Nat. Phys. **17**, 1413 (2021).

[15] Persky, E. et al. Magnetic memory and spontaneous vortices in a van der waals superconductor. Nature **607**, 692 (2022).

[16] Silber, I. et al. Two-component nematic superconductivity in 4Hb-TaS_2. Nat. Commun. **15**, 824 (2024).

[17] Almoalem, A. et al. The observation of π-shifts in the LittleParks effect in 4Hb-TaS_2. Nat. Commun. **15**, 4623 (2024).

[18] Gao, J. J. et al. Origin of the large magnetoresistance in the candidate chiral superconductor $4H_b{-}TaS_2$. Phys. Rev. B **102**, 075138 (2020).

[19] Meng, F. et al. Extreme orbital ab-plane upper critical fields far beyond the Pauli limit in $4H_b$-Ta(S, Se)$_2$ bulk crystals. Phys. Rev. B **109**, 134510 (2024).

[20] Meyer, S. F., Howard, R. E., Stewart, G. R., Acrivos, J. V. & Geballe, T. H. Properties of intercalated 2H-$NbSe_2$, 4Hb-TaS_2, and 1T-TaS_2. The Journal of Chemical Physics **62**, 4411–4419 (1975). URL https://doi.org/10.1063/1.430342.

[21] Yang, Y. et al. Enhanced superconductivity upon weakening of charge density wave transport in 2H-TaS_2 in the two-dimensional limit. Phys. Rev. B **98**, 035203 (2018). URL https://link.aps.org/doi/10.1103/PhysRevB.98.035203.

[22] Almoalem, A. et al. Charge transfer and spin-valley locking in 4Hb-TaS_2. npj Quantum Mater. **9**, 36 (2024).

[23] Date, M. et al. Charge transfer empties the flat band in 4Hb-TaS_2 - except at the surface (2025). URL https://arxiv.org/abs/2508.16411. 2508.16411.

[24] Gofman, R. A. et al. Chiral charge density wave in 4Hb- and 1T-TaS_2: the role of interlayer coupling (2025). URL https://arxiv.org/abs/2508.16559. 2508.16559.

[25] Li, Y. et al. Interlayer Coupling Driven Correlated and Charge Ordered Electronic States in a Transition Metal Dichalcogenide Superlattice (2025). URL https://arxiv.org/abs/2511.14570. Version Number: 1.

[26] Sun, X. et al. Anomalous narrow-band correlation in a natural superconducting heterostructure (2025). URL https://arxiv.org/abs/2508.18099. 2508.18099.

[27] Watson, M. D. et al. Folded pseudochiral Fermi surface in 4Hb-$TaSe_2$ from band hybridization with a charge density wave. Communications Materials **6**, 24 (2025). URL https://www.nature.com/articles/s43246-025-00743-0.

[28] Yang, F. Z. et al. Charge density waves in the 2.5-dimensional quantum heterostructure. Phys. Rev. B **111**, L041101 (2025).

[29] Yang, F. Z. et al. Signature of magnetoelectric coupling driven finite momentum pairing in 3D ising superconductor. Nat. Commun. **16**, 6626 (2025).

[30] Shen, S. et al. Coexistence of Quasi-two-dimensional Superconductivity and Tunable Kondo Lattice in a van der Waals Superconductor. Chin. Phys. Lett. **39**, 077401 (2022). URL https://iopscience.iop.org/article/10.1088/0256-307X/39/7/077401.

[31] Yan, S. et al. Influence of domain walls in the incommensurate charge density wave state of Cu intercalated 1T-$TiSe_2$. Phys. Rev. Lett. **118**, 106405 (2017).

[32] Wang, Z. et al. Evidence for dispersing 1D Majorana channels in an iron-based superconductor. Science **367**, 104 (2020).

[33] Fazekas, P. & Tosatti, E. Charge carrier localization in pure and doped 1T-TaS_2. Physica B+C **99**, 183–187 (1980). URL https://linkinghub.elsevier.com/retrieve/pii/0378436380902296.

[34] Petocchi, F. et al. Mott versus Hybridization Gap in the Low Temperature Phase of 1T-TaS_2. Phys. Rev. Lett. **129**, 016402 (2022). URL https://link.aps.org/doi/10.1103/PhysRevLett.129.016402.

[35] Chen, Y. et al. Strong correlations and orbital texture in single-layer 1T-$TaSe_2$. Nat. Phys. **16**, 218–224 (2020). URL https://www.nature.com/articles/s41567-019-0744-9.

[36] Lin, H. et al. Scanning tunneling spectroscopic study of monolayer 1T-TaS_2 and 1T-$TaSe_2$. Nano Research **13**, 133–137 (2020). URL https://doi.org/10.1007/s12274-019-2584-4.

[37] Bovet, M. et al. Pseudogapped fermi surfaces of 1T-TaS_2 and 1T-$TaSe_2$: A charge density wave effect. Phys. Rev. B **69**, 125117 (2004). URL https://link.aps.org/doi/10.1103/PhysRevB.69.125117.

[38] Ang, R. et al. Superconductivity and bandwidth-controlled Mott metal-insulator transition in 1T-$TaS_{2-x}Se_x$. Phys. Rev. B **88**, 115145 (2013). URL https://link.aps.org/doi/10.1103/PhysRevB.88.115145.

[39] Darancet, P., Millis, A. J. & Marianetti, C. A. Three-dimensional metallic and two-dimensional insulating behavior in octahedral tantalum dichalcogenides. Physical Review B **90**, 045134 (2014). URL https://link.aps.org/doi/10.1103/PhysRevB.90.045134.

[40] Fleming, R. M. Oscillatory magnetotransport in the layer compounds 4Hb-TaS_2 and 2H-$TaSe_2$. Phys. Rev. B **16**, 302–315 (1977).

[41] Petrović, A. P. et al. A disorder-enhanced quasi-one-dimensional superconductor. Nature Communications **7**, 12262 (2016). URL https://www.nature.com/articles/ncomms12262.

[42] Fan, B. & García-García, A. M. Superconductivity at the three-dimensional Anderson metal-insulator transition. Physical Review B **102**, 184507 (2020). URL https://link.aps.org/doi/10.1103/PhysRevB.102.184507.

[43] Gastiasoro, M. N. & Andersen, B. M. Enhancing superconductivity by disorder. Physical Review B **98**, 184510 (2018). URL https://link.aps.org/doi/10.1103/PhysRevB.98.184510.

[44] Li, C. et al. Strange Metal and Superconductor in the Two-Dimensional Yukawa-Sachdev-Ye-Kitaev Model. Physical Review Letters **133**, 186502 (2024). URL https://link.aps.org/doi/10.1103/PhysRevLett.133.186502.

[45] Sacépé, B. et al. Localization of preformed Cooper pairs in disordered superconductors. Nature Physics **7**, 239–244 (2011). URL https://www.nature.com/articles/nphys1892.

[46] Chen, L. et al. Planar thermal Hall effect from phonons in a Kitaev candidate material. Nat. Commun. **15**, 3513 (2024).

[47] Chen, L. et al. Planar thermal Hall effect from phonons in cuprates. Phys. Rev. X **14**, 041011 (2024).

[48] Liu, G.-B., Shan, W.-Y., Yao, Y., Yao, W. & Xiao, D. Three-band tight-binding model for monolayers of group-VIB transition metal dichalcogenides. Phys. Rev. B **88**, 085433 (2013). URL https://link.aps.org/doi/10.1103/PhysRevB.88.085433.

[49] Geng, Y. et al. Correlated electrons in the flat band in the charge density wave state of $4H_b-TaSe_xS_{2-x}$. Phys. Rev. B **110**, 115107 (2024).

[50] Yang, W. et al. Nanoscale modulation of flat bands via controllable charge density wave defects in 4Hb-TaS_2. Phys. Rev. B **112**, 245126 (2025). URL https://link.aps.org/doi/10.1103/lw6k-m6df.

[51] Moser, S. An experimentalist's guide to the matrix element in angle resolved photoemission. Journal of Electron Spectroscopy and Related Phenomena **214**, 29–52 (2017). URL http://www.sciencedirect.com/science/article/pii/S0368204816301724.

[52] Núñez Regueiro, M. D., Lopez-Castillo, J. M. & Ayache, C. Thermal conductivity of 1T-TaS_2 and 2H-TaS_2. Phys. Rev. Lett. **55**, 1931 (1985).

[53] Chen, L., Boulanger, M.-E., Wang, Z.-C., Tafti, F. & Taillefer, L. Large phonon thermal Hall conductivity in the antiferromagnetic insulator Cu_3TeO_6. Proc. Natl. Acad. Sci. U.S.A. **119**, e2208016119 (2022).

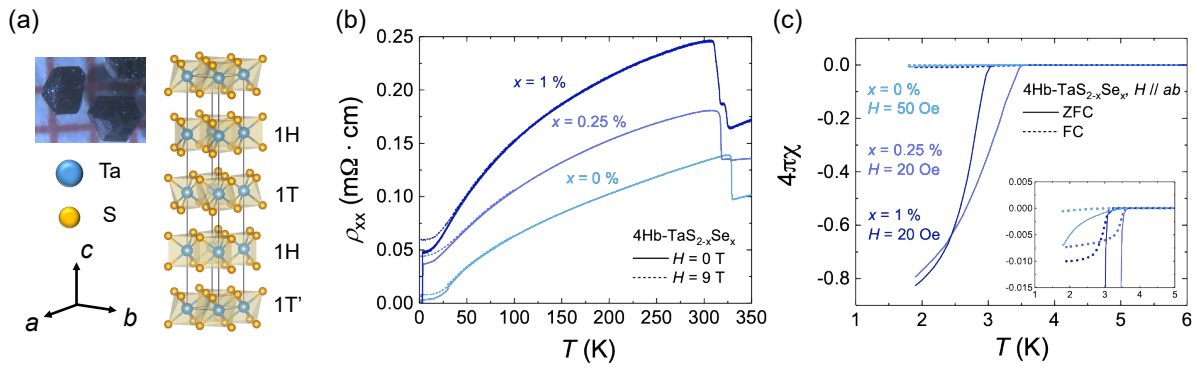


Figure 1: **Sensitivity of superconductivity to Se substitution.** (a) Crystal structure of $4Hb$-Ta$(S_{1-x}Se_x)_2$. $1T$-$TaS_{2-x}Se_x$ and $1H$-$TaS_{2-x}Se_x$ layers stack along the crystal c axis with van der Waals coupling between the layers. Single crystals of $4Hb$-Ta$(S_{1-x}Se_x)_2$ are also shown. (b) Temperature dependence of the in-plane electrical resistivity $\rho_{xx}(T)$ for $4Hb$-Ta$(S_{1-x}Se_x)_2$ single crystals with three different Se concentrations at magnetic fields of H = 0 T (solid line) and H = 9 T (short dashed line). The $x = 0\%$ sample shows a clear kink in resistivity around $T \sim 30$ K due to the appearance of a 3×3 commensurate charge density wave (CCDW) in the 1H layer. This low-temperature CCDW transition is obscured in the $x = 0.25\%$ and $x = 1\%$ samples due to disorder. (c) Temperature dependence of the magnetic susceptibility in three $4Hb$-Ta$(S_{1-x}Se_x)_2$ single crystals with different Se concentration: $x = 0\%$, $x = 0.25\%$, and $x = 1\%$. Inset shows a zoom-in view of $4\pi\chi(T)$ curves. The superconducting volume fraction (SCVF) is only 0.6% for the $x = 0\%$ sample, while it is greatly enhanced to about 80% for the $x = 0.25\%$ and $x = 1\%$ samples.

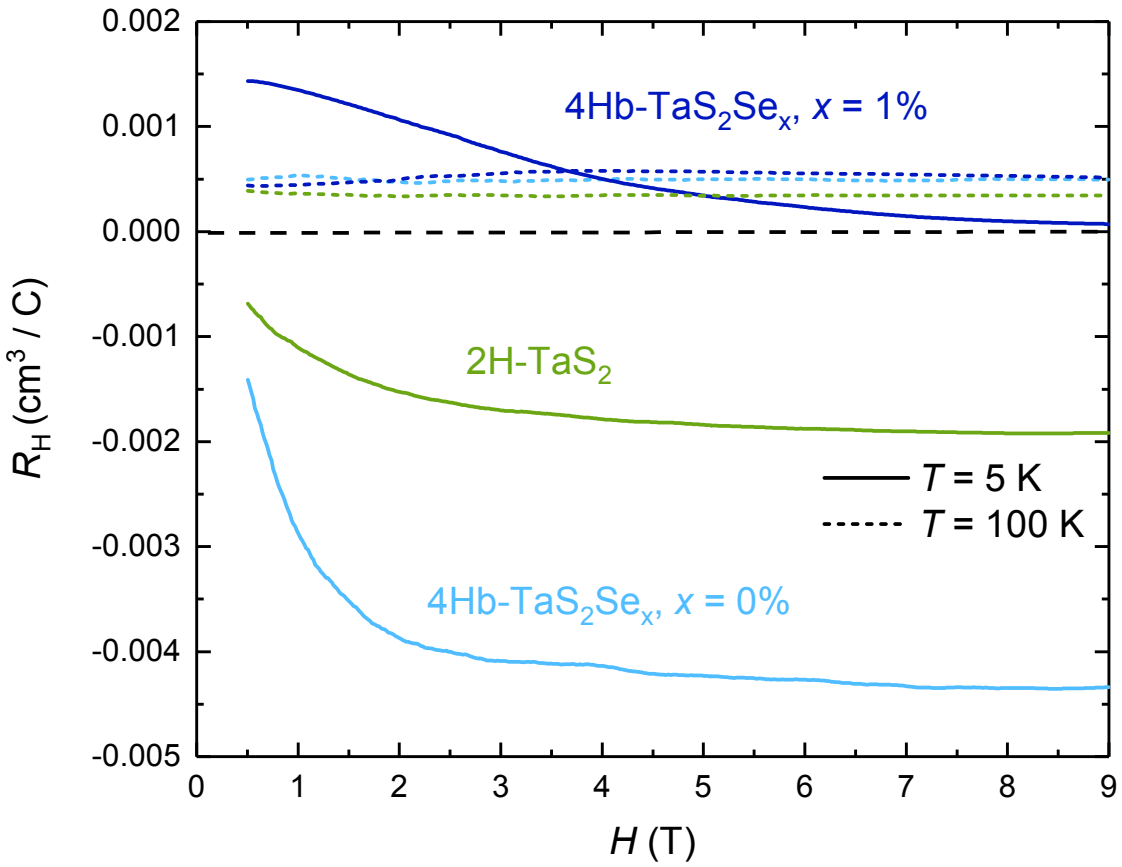


Figure 2: **Evidence for delocalization transition in 4Hb-Ta(S$_{1-x}$Se$_x$)$_2$ as a function of Se substitution.** Hall coefficient $R_{\rm H}$ in the high field limit at low temperature (5 K, solid lines) and high temperature (100 K, dashed lines) measured in 2H-TaS$_2$ (green curves) and 4Hb-Ta(S$_{1-x}$Se$_x$)$_2$ samples at $x = 0\%$ (light blue curves) and 1% (dark blue curves). At all temperatures the 4Hb-Ta(S$_{1-x}$Se$_x$)$_2$ $x = 0\%$ sample has roughly half the carriers of 2H-TaS$_2$, consistent with all the carriers in the 1T layers being localized. At low temperatures the 4Hb-Ta(S$_{1-x}$Se$_x$)$_2$ at $x = 1\%$ sees a dramatic change where the Hall coefficient not only changes sign, but asymptotes to a small value of R$_H$, suggesting a huge increase in carrier density.

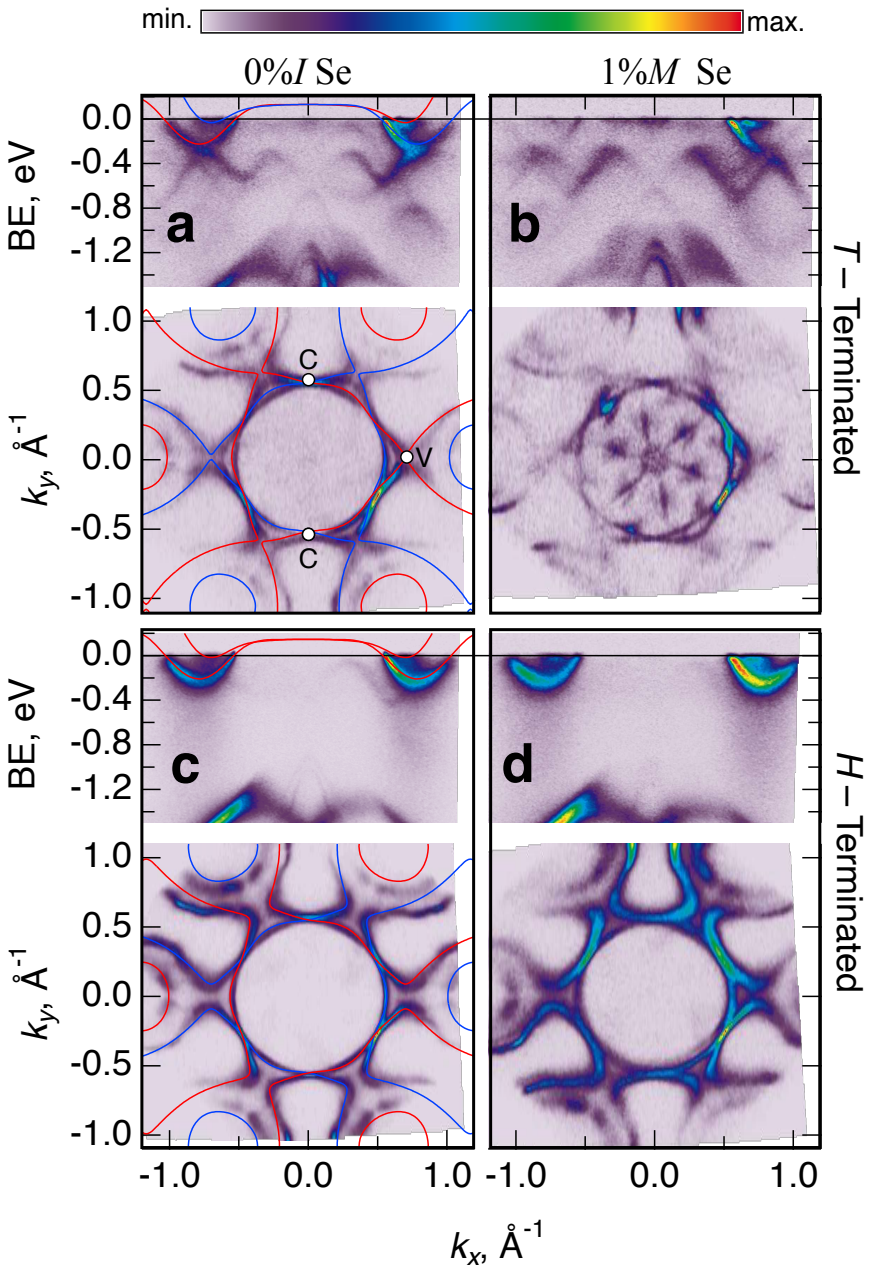


Figure 3: **ARPES evidence for a delocalization transition in 4Hb-Ta(S$_{1-x}$Se$_x$)$_2$.** Slices of the full ARPES Binding Energy (BE) *vs.* **k** data set for (a,b) 1T-terminated and (c,d) 1H-terminated regions of the sample surface. The upper part of each panel is a bandstructure slice (BE *vs.* k_x at $k_y = 0$, while the lower part is the intensity distribution at $E_{\rm F}$ along k_x and k_y. The ARPES data shows the same dramatic effect as the electrical Hall effect: there is a filling of the CDW gap in the 1H layers (red circles) while in the 1T layer a metallic Fermi surface appears near Γ with 1% Se substitution. The data are collected at photon energy 72 eV, and all panels use the same color scale linearly mapped onto the individual intensity ranges.

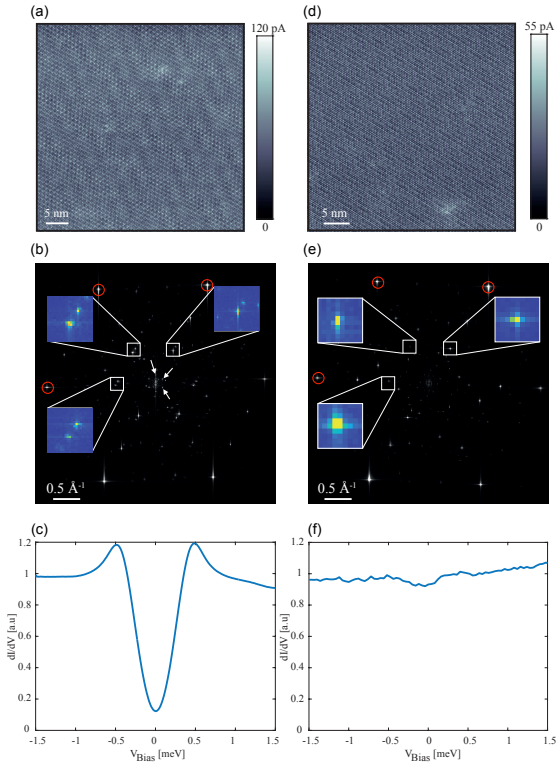


Figure 4: **Correlation between the SC-gap and CDW domains in pristine 4Hb-TaS_2.** (a) Atomically resolved topography of the $1H$ layer ($V = -5$ mV, $I = 70$ pA). (b) Fast Fourier transform (FFT) of the topography in (a), with white arrows indicating central moiré peaks. (c) Averaged tunneling spectrum acquired on the surface shown in (a), displaying a well-defined superconducting gap (V_{set} = -1.5 mV, I = 70 pA, $V_{\text{modulation}}$ = 30 μeV). (d, e) Topography and corresponding FFT at a different location showing unsplit CDW peaks. (f) Averaged spectrum in the region shown in (d), indicating a highly suppressed gap (V_{set} = -2 mV, I = 100 pA, $V_{\text{modulation}}$ = 40 μeV). Spectra in (c) and (f) were taken with the same tip on the same sample. All measurements were obtained at $T \sim 300$ mK.

Supplementary Files

This is a list of supplementary files associated with this preprint. Click to download.

- ChenBulkSCSupp.pdf